Astronomy & Astrophysics manuscript no. main
December 20, 2016

Super-sample covariance approximations and partial sky coverage

Fabien Lacasa[1⋆], Marcos Lima[2], and Michel Aguena[2]

[1] Département de Physique Théorique, Université de Genève, 24 quai Ernest Ansermet, CH-1211 Geneva, Switzerland
[2] Departamento de Física Matemática, Instituto de Física, Universidade de São Paulo, CP 66318, CEP 05314-970, São Paulo-SP, Brazil

December 20, 2016

ABSTRACT

Super-sample covariance (SSC) is the dominant source of statistical error on large scale structure observables for both current and future galaxy surveys. In this work, we concentrate on the SSC of cluster counts, also known as sample variance, which is particularly useful for the self-calibration of the cluster observable-mass relation; our approach can similarly be applied to other observables, such as galaxy clustering and lensing shear. We first examine the accuracy of two analytical approximations proposed in the literature for the flat sky limit, finding that they are accurate respectively at the 15% and 30-35% level for covariances of counts in the same redshift bin. We then develop a harmonic expansion formalism that allows for the prediction of SSC in an arbitrary survey mask geometry, such as large sky areas of current and future surveys. We show analytically and numerically that this formalism recovers the full sky and flat sky limits present in the literature. We then present an efficient numerical implementation of the formalism, which allows fast and easy runs of covariance predictions when the survey mask is modified. We apply our method to a mask broadly similar to the Dark Energy Survey footprint, finding a non-negligible negative cross-z covariance, i.e. redshift bins are anti-correlated. We also examine the case of data removal from holes due e.g. to bright stars, quality cuts or systematic removals, and find that this does not have noticeable effects on the structure of the SSC matrix, only rescaling its amplitude by the effective survey area. These advances make possible for current and future galaxy surveys the computation of cosmology-dependent theoretical covariances, which can improve parameter constraints compared to methods that fix the covariance from data or simulations.

Key words. large scale structure of the universe - methods: analytical

1. Introduction

The large scale structure of the universe results from the growth of local density perturbations induced by gravitational collapse within an expanding background (e.g. Peebles 1980). The multi-point correlations and associated spectra that characterize this structure can be measured in real data and combined with theory predictions, in order to constrain cosmological models – including gravity theories and relative amounts of dark matter and dark energy (Astier et al. 2006; Percival et al. 2010; Riess et al. 2009; Hildebrandt et al. 2016; Beutler et al. 2017; Hinton et al. 2017). However, likelihood methods of parameter inference also require reliable estimates of the covariances associated to structure observables. Estimates of the covariances can be obtained from the actual data via methods such as jackknife and bootstrap; from simulations and Monte Carlo realizations; and from theoretical predictions which account for the known observational effects (Dodelson & Schneider 2013; Giannantonio et al. 2016; Crocce et al. 2016; O'Connell et al. 2016; Singh et al. 2016; Shirasaki et al. 2016; Blot et al. 2016; Escoffier et al. 2016; Pearson & Samushia 2016; Camacho et al. in prep.). In this work we focus on the latter approach.

Within the so-called halo model paradigm (Cooray & Sheth 2002), large scale structure can be characterized by the statistical properties of the universe building blocks, i.e. dark matter halos. These halos are characterized by their abundance, bias and profiles, all of which can be studied from dark matter N-body simulations and also from high-quality data sets. As galaxy clusters develop within dark matter halos, they trace the highest density peaks. Their number counts and covariances are very sensitive probes of structure growth and expansion of the Universe (Lima & Hu 2004, 2005, 2007; Schmidt et al. 2009; Aguena & Lima 2016). A number of past and current surveys have detected clusters in multiple wavelengths with hopes to use them for cosmological purposes (Miller et al. 2005; Koester et al. 2007; Soares-Santos et al. 2011; Dietrich et al. 2014; Rykoff et al. 2014; Bleem et al. 2015; Planck Collaboration et al. 2016; Rykoff et al. 2016; Bayliss et al. 2016).

As we consider scales close to the survey maximum size, the number of modes available decrease significantly, which represents an intrinsic source of uncertainty for the inferred structure properties. The sample covariance quantifies these uncertainties and may have contributions from scales much larger than the survey itself, in which case we refer to it as super-sample covariance (SSC), whose effects have been studied recently in multiple contexts (e.g Takada & Hu 2013; Li et al. 2014a,b; Takahashi et al. 2014; Li et al. 2016;

⋆ fabien.lacasa@unige.ch

Shirasaki et al. 2016; Hu et al. 2016), and has been shown to be particularly important for probe combinations as it couples observables together (Takada & Bridle 2007; Takada & Spergel 2014; Krause & Eifler 2016; Lacasa & Rosenfeld 2016). Within a local patch, large scale modes change the effective average density, which can differ significantly and unpredictably from the true background density, affecting the inferred correlations. This effect becomes more important for small survey areas, but is relevant even for observations of the full sky due to super-horizon modes. In fact, SSC may be the dominant source of errors on Jackknife covariance estimations (Shirasaki et al. 2016).

Finally, the survey geometry or footprint as well as its selection function – characterized e.g. by masks and depth maps – also affect the estimation of correlations and covariances (Takahashi et al. 2014). Not only the geometry and selection must be known to good precision, but their properties must be properly propagated into the measured and predicted correlations and covariances. Some predictions can only be directly made under certain approximations, e.g. for full sky calculations, while for the more realistic case of partial sky coverage, further complicating assumptions need to be made. As we attempt to extract maximum information from observations, we may end up with a complicated survey mask containing holes (e.g. due to saturated pixels, asteroids, contamination from stars, or simply pixels that do not satisfy a depth criterion). All these effects must be accounted for in a proper cosmological analysis.

In this article, we study the effect of partial sky coverage and arbitrary masks in the estimation of the super-sample covariance of cluster counts. We propose a method to estimate this covariance efficiently for an arbitrary mask, and compare this approach to a number of approximated calculations in the literature. We show that our general calculation reduces to the approximated computations in the appropriate limits, but differ from them in general. Although beyond the scope of this work, we expect our theoretical estimation can be compared to other methods of estimating the covariance which also attempt to account for the survey geometry and mask effects, such as Jackknife methods or simulation realizations. The main advantage of our method though is that it allows for the covariance to be computed as a function of cosmology at each step of a monte carlo markov chain, therefore avoiding problems e.g. from fixing the covariance at an incorrect cosmology. Allowing for the variation of the covariance with cosmological and *nuisance* parameters allows e.g. for self-calibration of cluster observable-mass distribution in general cosmological analyses of cluster samples (Lima & Hu 2005).

This article is organised as follows. In Sect. 2, we introduce the SSC formalism for SSC full equations in the case of cluster counts, and consider the limits of flat sky (small angles) and full sky, providing some comparisons for the covariance kernels in these approximations. In Sect. 3 we consider the flat sky limit under different approximations which have been proposed in the literature for computing the SCC, and compare them to the full exact computation. In Sect. 4, we propose a method to numerically compute SSC in the case of partial sky coverage with an arbitrary survey mask. In Sect. 5 we present our results, applying the method to the case of a geometry similar to that of Dark Energy Survey (DES), discussing the mask effects, and recovering the flat sky limit. Finally, in Sect. 6 we present our conclusions and perpectives.

In all numerical computations, we take a cosmology for a flat ΛCDM universe with parameter values $h = 0.67$, $\Omega_b h^2 = 0.022$, $\Omega_c h^2 = 0.12$, $w = -1$, $n_S = 0.96$, $\sigma_8 = 0.83$. Cluster counts are computed in two bins of redshift in the range $z \in [0.4, 0.6]$ with $\Delta z = 0.1$, and four bins of mass in the range $\log[M/(h^{-1}M_\odot)] \in [14, 16]$ with $\Delta \log[M/(h^{-1}M_\odot)] = 0.5$. The halo mass function is from a fit to simulations from Tinker et al. (2008), the halo bias is from Tinker et al. (2010) and the linear matter power spectrum is from the transfer function by Eisenstein & Hu (1998). We set the following notational conventions: $r(z)$ is the comoving distance i.e. $dr = dz/H(z)$ with $H(z)$ the Hubble parameter, and $\mathrm{d}V = r^2 dr$ is the comoving volume element per steradian. We use shortcuts such as $\mathrm{d}X_{12} = \mathrm{d}X_1\,\mathrm{d}X_2$ and $P(k|z_{12}) = P(k|z_1, z_2) = G(z_1)G(z_2)P(k)$ with $G(z)$ the linear growth function. Often the limits of redshift/mass integrals are implicitly those of the redshift/mass bin considered.

2. Super-sample covariance

Super-sample covariance (SSC) is a source of uncertainties for large scale structure (LSS) observables, coming from modes of size larger than the survey. The effect of these large scale modes on structure comes from the fact that the effective or local matter density $\bar{\rho}_m^{\rm eff}(z)$ averaged within the survey can be different from the true background density $\bar{\rho}_m(z)$ averaged over the whole universe or an ensemble of universes:

$$\bar{\rho}_m^{\rm eff}(z) = \bar{\rho}_m(z)[1 + \delta_b'(z)]\,, \tag{1}$$

where $\delta_b'(z)$ is a background density perturbation induced by large scale modes. Defining the density contrasts

$$\delta_m(\mathbf{x}) = \frac{\rho(\mathbf{x}) - \bar{\rho}_m}{\bar{\rho}_m} \qquad \text{and} \qquad \delta_m^{\rm eff}(\mathbf{x}) = \frac{\rho(\mathbf{x}) - \bar{\rho}_m^{\rm eff}}{\bar{\rho}_m^{\rm eff}}\,, \tag{2}$$

the ensemble average $\langle \delta_m(\mathbf{x}) \rangle = 0$ whereas the spatial average $\langle \delta_m^{\rm eff}(\mathbf{x}) \rangle = \delta_b'/(1 + \delta_b') \equiv \delta_b \approx \delta_b'$.

We split the survey window function $W(\mathbf{x})$ into radial $W(z)$ and angular $W(\hat{\mathbf{n}})$ pieces, i.e. $W(\mathbf{x}) = W(z)W(\hat{\mathbf{n}})$. The radial part simply specifies the redshift binning and will often be suppressed in our description below, where it will be effectively included within integration limits. On the other hand, the angular window $W(\hat{\mathbf{n}})$ is the main object whose effect on the covariances we want to consider. In principle $W(\hat{\mathbf{n}})$ may depend on redshift as well. In fact, this is very often the case for surveys with significant depth variations across the sky. For simplicity, we will keep the angular window only as a function of the angular vector, though the formalism can be easily generalized (see Appendix A).

If the survey angular window $W(\hat{\mathbf{n}})$ subtends a solid angle Ω_S in the sky, and we denote the position vector $\mathbf{x} = r(z)\hat{\mathbf{n}}$, the background perturbation δ_b is given by

$$\delta_b(z) = \frac{1}{\Omega_S} \int \mathrm{d}^2\hat{\mathbf{n}}\, W(\hat{\mathbf{n}})\, \delta_m(r(z)\hat{\mathbf{n}}, z)\,. \tag{3}$$

As a result, all LSS observables will respond to such change of background density, becoming correlated. Explicitly, the SSC term of the cross-covariance between two observables $\mathcal{O}_1$ and $\mathcal{O}_2$ is given by (e.g. Lacasa & Rosenfeld 2016) :

$$\mathrm{Cov}^{\rm SSC}(\mathcal{O}_1, \mathcal{O}_2) = \int \mathrm{d}V_{12}\, \frac{\partial \mathfrak{o}_1}{\partial \delta_b}\, \frac{\partial \mathfrak{o}_2}{\partial \delta_b}\, \sigma^2(z_1, z_2)\,, \tag{4}$$

where $\mathfrak{o}_i$ is the density of observable $\mathcal{O}_i$ (per comoving volume dV), $\partial\mathfrak{o}_i/\partial\delta_b$ is its reaction to the change in background δ_b, and $\sigma^2(z_1, z_2)$ is the covariance of δ_b :

$$\sigma^2(z_1, z_2) = \langle \delta_b(z_1)\, \delta_b(z_2) \rangle = \int \frac{\mathrm{d}^3\mathbf{k}}{(2\pi)^3}\, \tilde{W}^2(\mathbf{k})\, P(k|z_{12})\,, \tag{5}$$

with $\tilde{W}$ the Fourier transform of the survey window function.

In this article, we will be mostly interested in the case of cluster number counts $N_{\rm cl}(i_M, i_z)$ per steradian within bins of mass i_M and bins of redshift i_z [1],

$$N_{\rm cl}(i_M, i_z) = \int_{z\in \mathrm{bin}(i_z)} \mathrm{d}V \int_{M\in\mathrm{bin}(i_M)} \mathrm{d}M\, \frac{\mathrm{d}n_h(z, M)}{\mathrm{d}M}\,, \tag{6}$$

where dn_h/dM is the halo mass-function. The super-sample covariance of these counts is traditionally denoted simply as sample covariance in the cluster literature. It is important to notice though that super-horizon modes affect even full sky surveys and must always be accounted for. The SSC for clusters counts is given by (e.g. Lacasa & Rosenfeld 2016) :

$$\mathrm{Cov}^{\rm SSC}(N_{\rm cl}(i_M, i_z), N_{\rm cl}(j_M, j_z)) = \int \mathrm{d}V_{12}\, \frac{\partial n_h}{\partial\delta_b}(i_M, z_1)\, \frac{\partial n_h}{\partial\delta_b}(i_M, z_2)\, \sigma^2(z_1, z_2)\,, \tag{7}$$

where the response of the halo number density $n_h = dN_{\rm cl}/dV$ to a change of background density is given by the number-weighted halo-bias averaged within the bin (e.g. Schmidt et al. 2013) :

$$\frac{\partial n_h}{\partial\delta_b}(i_M, z) = \int_{M\in\mathrm{bin}(i_M)} \mathrm{d}M\, \frac{\mathrm{d}n_h}{\mathrm{d}M}\, b(M, z)\,, \tag{8}$$

where $b(M, z)$ is the (first order) halo bias.

Most of the elements for the computation of the covariance pose no particular numerical problem. A notable exception is $\sigma^2(z_1, z_2)$, as it depends on the survey geometry. Numerically tractable formulae are known only for a few cases with simple geometries. First, for the case of full sky, we have (Lacasa & Rosenfeld 2016) :

$$\sigma^2_{\rm fullsky}(z_1, z_2) = \frac{1}{2\pi^2} \int k^2\, \mathrm{d}k\, j_0(kr_1)\, j_0(kr_2)\, P_m(k|z_{12})\,, \tag{9}$$

where $r_i = r(z_i)$. Second, an expression for $\sigma^2(z_1, z_2)$ is also known in the flat sky limit (e.g. Hu & Kravtsov 2003; Lima & Hu 2007; Aguena & Lima 2016) :

$$\sigma^2_{\rm flatsky}(z_1, z_2) = \frac{1}{2\pi^2} \int k_\perp\, \mathrm{d}k_\perp\, 4 \frac{J_1(k_\perp\theta_S r_1)}{k_\perp\theta_S r_1} \frac{J_1(k_\perp\theta_S r_2)}{k_\perp\theta_S r_2} \times \int \mathrm{d}k_\parallel\, \cos\left[k_\parallel(r_1 - r_2)\right]\, P(k|z_{12})\,, \tag{10}$$

[1] Throughout this article $N_{\rm cl}$ is the number of clusters per steradian. For application to a survey, $N_{\rm cl}$ and its covariance may be re-scaled by the observed area.

for a cylindrical window function of radius θ_S delineating a survey solid angle $\Omega_S = 2\pi(1-\cos\theta_S) \approx \pi\theta_S^2$, and the wavevector $\mathbf{k} = (k_\parallel, k_\perp)$ is split into its components parallel and perpendicular to the line of sight, with $k^2 = k_\perp^2 + k_\parallel^2$.

Fig. 1 shows the comparison of σ^2 resulting from the two expressions above for an angular window of radius $\theta_S = 5$ deg. The full sky covariance was re-scaled by a factor $f_{\rm SKY}^{-1}$ – where $f_{\rm SKY} = \Omega_S/4\pi$ and $\Omega_S = \pi\theta_S^2$ – an approximation usually made for covariances in partial sky. We see that

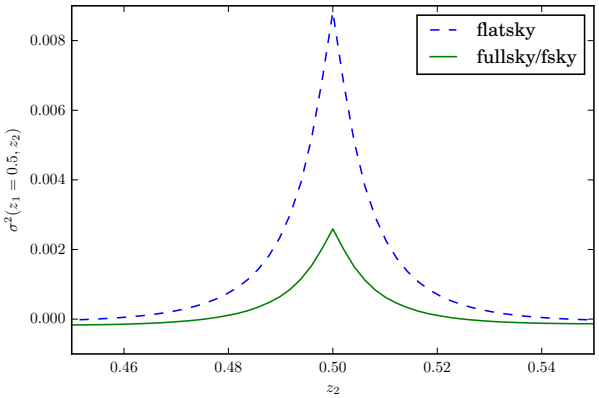

Fig. 1. Comparison of $\sigma^2(z_1, z_2)$ for $z_1 = 0.5$ in different cases. In blue the flat sky formula Eq. 10 for a survey angular radius $\theta_S = 5$ deg. In green the full sky formula Eq. 9, rescaled by a factor $1/f_{\rm SKY}$.

both covariances share the behaviour of peaking at $z_1 = z_2$ and decreasing to zero as $|z_1 - z_2|$ increases[2]. Regarding the amplitudes, we see that re-scaling the full sky covariance by the usual $1/f_{\rm SKY}$ factor underpredicts the covariance by a factor ~ 3.4 in this case[3]. Even when re-scaling by hand the covariances to the same peak amplitude, we find that their shapes are broadly similar but differ in details. The full sky covariance is more strongly peaked at the center, then decreases and crosses zero, reaching a negative minima of height $\sim 7\%$ of its peak, before slowly asymptoting zero. By contrast, the flat sky covariance is a bit broader in its positive part, but its negative minimum is only $\sim 0.8\%$ of its peak, and it asymptotes faster to zero. This clearly indicates that super-sample covariance is non-trivially related to sky coverage, and a more general approach is required for its accurate computation.

3. Comparison of SSC approximations

The full equation Eq. 7 for SSC can be numerically expensive, as it requires a double redshift integral. Furthermore, for each pair of redshift, a double $(k_\perp, k_\parallel)$ integral is required (e.g. in the flat sky case). To tame down this burden, several approximations have been devised in the literature. Below we consider two approximations in the flat sky regime.

[2] By eye, both functions seem symmetric around $z_1 = z_2$, but in detail this is not true.

[3] An artificial factor $1/f_{\rm SKY}^2$ would not fare better, this time overpredicting the covariance.

First, in Eq. 7 we can assume that $\partial n_h/\partial\delta_b$ varies slowly with within the bins, such that it can be approximated by its value at the bin centroid and taken out of the integral. In fact this may be a good approximation for sufficiently narrow bins. In this case, Eq. 7 takes the form (Hu & Kravtsov 2003)

$$\mathrm{Cov}^{\mathrm{SSC}}(N_{\mathrm{cl}}(i_M,i_z),N_{\mathrm{cl}}(j_M,j_z)) \approx N_{\mathrm{cl}}(i_M,i_z)\,b(i_M,i_z)\;N_{\mathrm{cl}}(j_M,j_z)\,b(j_M,j_z)\,S_{i_z,j_z}\,, \tag{11}$$

where

$$S_{i_z,j_z} = \int \frac{\mathrm{d}V_{12}}{V_{12}}\;\sigma^2(z_1,z_2)\,, \tag{12}$$

and the normalized number-weighted halo bias within the bin is

$$b(i_M,i_z) = \frac{1}{n_h}\int_{M\in\mathrm{bin}(i_M)}\mathrm{d}M\,\frac{\mathrm{d}n_h}{\mathrm{d}M}\,b(M,\bar{z}_i)\,, \tag{13}$$

$$n_h = \int_{M\in\mathrm{bin}(i_M)}\mathrm{d}M\,\frac{\mathrm{d}n_h}{\mathrm{d}M}\,. \tag{14}$$

In fact, $b(i_M,i_z)$ is the cluster bias averaged in the mass bin, and taken at the center of the redshift bin $i_z=[z_i,z_{i+1}]$, i.e. $\bar{z}_i=(z_i+z_{i+1})/2$. This implicitly assumes that $b(M,z)$ varies slowly with z within the bin i_z. For a cylindrical window function of height δr in the flat sky case, the sample variance matrix S_{i_z,j_z} takes the form (Hu & Kravtsov 2003; Lima & Hu 2007; Aguena & Lima 2016)

$$S_{i_z,j_z} = \frac{1}{2\pi^2}\int k_\perp\,\mathrm{d}k_\perp\;4\;\frac{J_1(k_\perp\theta_S r_1)}{k_\perp\theta_S r_1}\;\frac{J_1(k_\perp\theta_S r_2)}{k_\perp\theta_S r_2} \times\int \mathrm{d}k_\parallel\;j_0\left(\frac{k_\parallel\delta r_1}{2}\right)j_0\left(\frac{k_\parallel\delta r_2}{2}\right)\cos\left[k_\parallel(r_1-r_2)\right]P(k|z_{12})\,, \tag{15}$$

where the power spectrum $P(k|z_{12})$ is evaluated at the center of the respective redshift bins. A nice feature of this approximation is that it removes the need to compute a double redshift integral. Furthermore the double integral over $(k_\perp,k_\parallel)$ only needs to be computed n_z^2 times (where n_z is the number of redshift bins), instead of all redshift pairs (z_1,z_2) needed to compute the redshift integral otherwise. This speeds up considerably the computation of SSC. We will call this approximation the Sij method.

Second, another approximation used (e.g. Krause & Eifler 2016) is that $\sigma^2(z_1,z_2)$ is a Dirac delta function at $z_1=z_2$, so that the double redshift integral collapses into a single integral :

$$\mathrm{Cov}^{\mathrm{SSC}}(N_{\mathrm{cl}}(i_M,i_z),N_{\mathrm{cl}}(j_M,j_z)) \approx \delta_{i_z,j_z}\int \mathrm{d}V\,r^2(z)\,\frac{\partial n_h}{\partial\delta_b}(i_M,z)\,\frac{\partial n_h}{\partial\delta_b}(j_M,z)\,\sigma_b(\Omega_S,z)\,, \tag{16}$$

where, following notation from Krause & Eifler (2016), we have

$$\sigma_b(\Omega_S,z) = \int\frac{k_\perp\,\mathrm{d}k_\perp}{2\pi}\;P(k_\perp,z)\;\left[\frac{2J_1(k_\perp r(z)\theta_S)}{k_\perp r(z)\theta_S}\right]^2\,, \tag{17}$$

where $P(k_\perp,z)=P(k=k_\perp,z)$, and we note that the $k_\parallel$ integral has disappeared, and that σ_b has units of Mpc/h.

The assumption behind this approximation is that the 3D window function $W(\mathbf{x})$ is much wider in the radial direction than in the transverse one. Thus super-survey modes have $k_\parallel \ll k_\perp$, and $P(k)$ can be taken as approximately constant within the $k_\parallel$ integral of Eq. 10. We thus expect the approximation to fare better for wide redshift bins and small angles. By limiting the computation to equal redshift bins $i_z=j_z$, and reducing the multiple integrals to a single redshift and a single wave-vector $k_\perp$ integral, the approximation speeds up considerably the SSC computation. Hereafter, we will call this approximation the KE method.

We implemented numerically all three SSC methods: 1) full computation from Eqs. 4 and 10, 2) Sij approximation and 3) KE approximation. Comparing the covariances at auto-redshifts, $i_z=j_z$, we found that both the Sij and KE approximations underpredict the amplitude of the covariance, respectively by $30-35\%$ and by $\sim 15\%$. The fact that Sij underpredicts the covariance is conform to our intuition; indeed, by taking values at the center of the redshift bins, the approximation neglects the fact that the mass function and the matter power spectrum both grow with time, which makes their integral larger[4]. We checked that the Sij method and full computation are in much better agreement for smaller redshift bins, and indeed it can be seen analytically that they reduce to each other in the limit $\Delta z\to 0$.

Concerning cross-redshift covariances, the full computation gives a positive correlation between our two redshift bins, reaching $\sim 13\%$ at maximum. On the other hand we found that the Sij approximation predicts anti-correlation between the bins, reaching at maximum -16%n while the KE approximation predicts, by construction, zero correlation. We checked that the Sij method performs better as the redshift bin width decreases. For instance at $\Delta z=0.01$, the agreement with the full computation is very good.

In Fig. 2, we show two correlation matrices for cluster counts obtained from each of the three SSC computations: on top is the correlation corresponding to the total covariance (i.e. SSC + shot-noise), and at the bottom the correlation of the SSC term only. The data points are ordered with increasing mass then increasing redshift, i.e. 0 refers to the lowest mass bin ($14<\log M<14.5$) in the first redshift bin ($0.4<z<0.5$), 3 refers to the highest mass bin ($15.5<\log M<16$) still in the first redshift bin, and then we go to the second redshift bin ($0.5<z<0.6$).

For the total covariance, the matrices are plotted with a common color code from black=0 to white=1. This lets appreciate the amplitude of the predicted SSC, compared to the shot-noise (which is proportional to N_{cl}, and as such independent of the SSC computation). We can see on these plots the fact that, compared to the full computation, both the Sij and KE methods underpredict the covariance. The cross-redshift covariance is however not visible on these plots, and is better seen in the bottom matrices, where the color code goes negative and we see that the Sij method predicts a too high anti-correlation between the redshift bins, while the KE method predicts zero correlation and the full computation finds a positive correlation. We can also see on these bottom plots that the Sij method predicts 100% SSC

[4] e.g. $1/3=\int_0^1 x^2\mathrm{d}x > 1/2*\int_0^1 x\mathrm{d}x = 1/4$

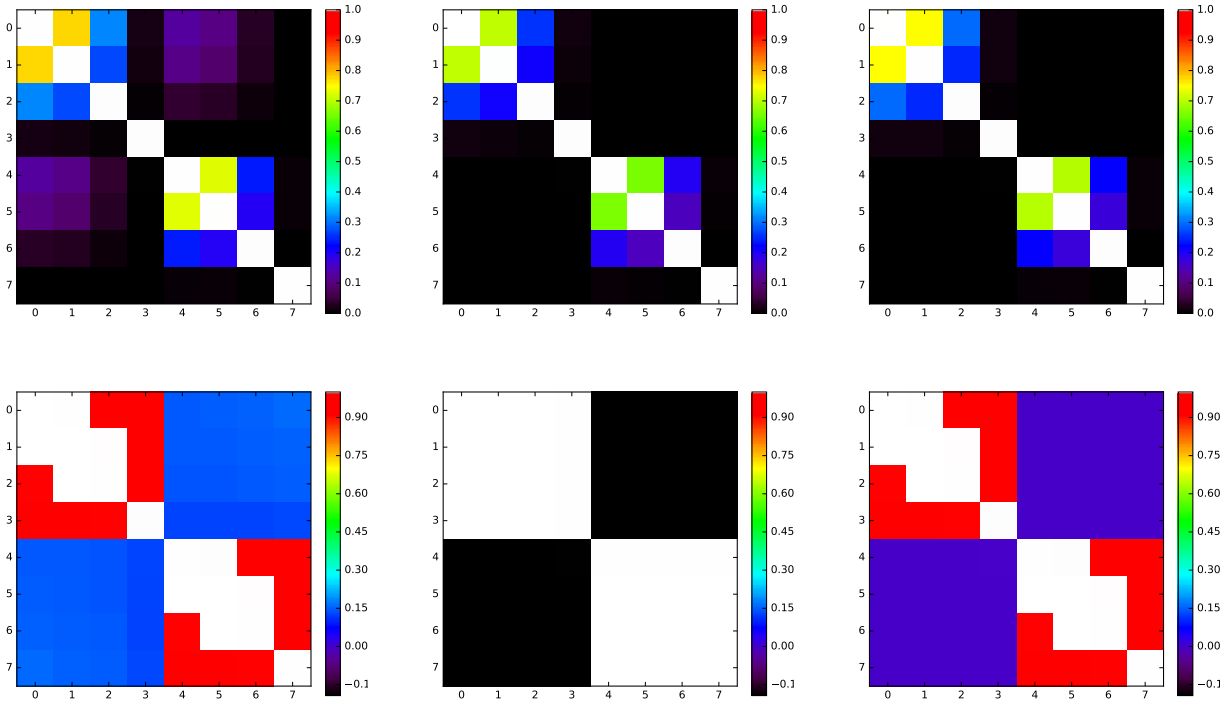

Fig. 2. Comparison of the cluster counts correlation matrix for different SSC computations, for a survey with angular radius $\theta_S = 5$ deg. The SSC matrix is displayed in 2 blocks for the redshift bins, and each block has 4 entries for the logarithmic mass bins. *Top:* correlation matrix of the total covariance (SSC+shot-noise) ; *Bottom:* correlation matrix of the SSC term only. *Left:* full numerical computation. *Center:* $S_{\rm i,j}$ approximation ; note that it has been cropped to [0,1], and otherwise goes negative (see text for details). *Right:* KE approximation. The color coding is such that white means 100%. Notice that for the top row the color code is from 0 to 1 while it goes negative in the bottom row (see text for details).

correlation between mass bins[5], while the full computation finds that the correlation goes down to 96%.

As a conclusion of this section, we see that the full computation is necessary to faithfully predict the SSC covariance matrix in the case $\Delta z = 0.1$. In fact, this is a representative binning for current photometric galaxy surveys whose present photo-z errors are of this order (e.g. Sánchez et al. 2014).

4. Super sample covariance for partial sky coverage

In this section, we will assume for simplicity that the survey mask is independent of redshift, as we in fact already did implicitly in Eq. 3. It is however straightforward to generalise the formalism to a redshift-dependent mask (see Appendix A).

4.1. Formal derivation

We want to compute the covariance of the background mode

$$\sigma^2(z_1, z_2) = \langle \delta_b(z_1)\, \delta_b(z_2) \rangle \ . \tag{18}$$

Given that the mask has zero value outside the survey, and given the normalisation of spherical harmonics such that $Y_{00} = 1/\sqrt{4\pi}$, the background mode of the survey is related to the monopole of the masked matter density as :

$$\delta_b(z) = \frac{1}{\sqrt{4\pi}\, f_{\rm SKY}}\, a_{00}^{\rm masked}(z)\,, \tag{19}$$

such that we have

$$\sigma^2(z_1, z_2) = \frac{1}{4\pi\, f_{\rm SKY}^2}\, \hat{C}_0^{\rm masked}(z_1, z_2)\,, \tag{20}$$

where $\hat{C}_0^{\rm masked}$ is the angular power spectrum at $\ell = 0$ of the masked matter density field. From C_ℓ pseudo-spectrum methods (e.g. Hivon et al. 2002), we know that the masked power spectrum is related to the true spectrum via the so-called coupling matrix, so that :

$$\hat{C}_0^{\rm masked}(z_1, z_2) = \sum_\ell \mathcal{M}_{0,\ell}\, C_\ell^{\rm true}(z_1, z_2)\,, \tag{21}$$

where $C_\ell^{\rm true}$ (hereafter simply $C_\ell^{\rm m}$) is the angular spectrum of matter density in an infinitesimal redshift shell. The coupling matrix is given by :

$$\mathcal{M}_{\ell_1,\ell_2} = (2\ell_2+1) \sum_{\ell_3} \frac{(2\ell_3+1)}{4\pi} \begin{pmatrix} \ell_1 & \ell_2 & \ell_3 \\ 0 & 0 & 0 \end{pmatrix}^2 C_{\ell_3}(W)\,, \tag{22}$$

where $C_\ell(W)$ is the angular power spectrum of the angular window $W(\hat{n})$. In our case, given the properties of Wigner

[5] these can be seen already analytically from Eq. 11

symbols, this simplifies to :

$$\mathcal{M}_{0,\ell} = \frac{(2\ell+1)^2}{4\pi} \begin{pmatrix} 0 & \ell & \ell \\ 0 & 0 & 0 \end{pmatrix}^2 C_\ell(W) \,. \tag{23}$$

Furthermore we have $\begin{pmatrix} 0 & \ell & \ell \\ 0 & 0 & 0 \end{pmatrix} = (2\ell+1)^{-1/2}$ and thus

$$\sigma^2(z_1, z_2) = \frac{1}{\Omega_{\rm S}^2} \sum_\ell (2\ell+1)\; C_\ell(W)\; C_\ell^{\rm m}(z_1, z_2) \,, \tag{24}$$

where $\Omega_{\rm S} = 4\pi\, f_{\rm SKY}$ and the matter angular power spectrum $C_\ell^{\rm m}$ is given by

$$C_\ell^{\rm m}(z_1, z_2) = \frac{2}{\pi} \int k^2\, {\rm d}k\; j_\ell(kr_1)\, j_\ell(kr_2)\; P(k|z_{12}) \,. \tag{25}$$

The combined Eqs. 24 and 25 represent the main analytical result of this article.

4.2. Limiting cases and remarks

It is interesting to examine a few limiting cases of Eqs. 24 and 25. In the full sky case, we have $C_\ell(W) = 4\pi\, \delta_{0,\ell}$ and $f_{\rm SKY} = 1$, and therefore thus we have

$$\sigma^2(z_1, z_2) = \sigma^2_{\rm fullsky}(z_1, z_2) = C_0^{\rm m}(z_1, z_2) \;/\; 4\pi \;, \tag{26}$$

recovering indeed Eq. 9.

In partial-sky, $C_0(W) = 4\pi\, f_{\rm SKY}^2$, so that

$$\sigma^2(z_1, z_2) = \sigma^2_{\rm fullsky}(z_1, z_2) + \frac{1}{\Omega_{\rm S}^2} \sum_{\ell \geq 1} (2\ell+1)\; C_\ell(W)\; C_\ell^{\rm m}(z_1, z_2) \,, \tag{27}$$

i.e. the full sky covariance term is the first in the sum contributing to the partial-sky covariance.

If $C_\ell^{\rm m}(z_1, z_2)$ is scale-independent, i.e. $C_\ell^{\rm m}(z_1, z_2) = C_0^{\rm m}(z_1, z_2)$ independently of ℓ (e.g. for $P(k|z_{12})$=constant, see Sect. 5.2), we have

$$\begin{aligned} \sigma^2(z_1, z_2) &= \sigma^2_{\rm fullsky}(z_1, z_2) \times \frac{1}{f_{\rm SKY}^2} \sum_\ell \frac{2\ell+1}{4\pi}\, C_\ell(W) \\ &= \sigma^2_{\rm fullsky}(z_1, z_2) / f_{\rm SKY} \,, \end{aligned} \tag{28}$$

and therefore $\mathrm{Cov}^{\rm SSC} = \mathrm{Cov}^{\rm SSC}_{\rm fullsky} / f_{\rm SKY}$, i.e. we obtain the usual $f_{\rm SKY}$ approximation to partial sky covariance. Conversely the reverse is also true: if the $f_{\rm SKY}$ approximation holds for any mask, then $C_\ell^{\rm m}(z_1, z_2)$ is constant. Given that for viable cosmological models $C_\ell^{\rm m}(z_1, z_2)$ is not constant, this shows that SSC is a non-trivial source of covariance that cannot be treated by classical approximations.

Now we notice that Eq. 24 can be rewritten as

$$\sigma^2(z_1, z_2) = \frac{1}{f_{\rm SKY}^2} \sum_\ell \frac{2\ell+1}{4\pi}\; C_\ell(W)\; \sigma_\ell^2(z_1, z_2) \,, \tag{29}$$

with

$$\begin{aligned} \sigma_\ell^2(z_1, z_2) &= \frac{C_\ell^{\rm m}(z_1, z_2)}{4\pi} \\ &= \frac{1}{2\pi^2} \int k^2\, {\rm d}k\; j_\ell(kr_1)\, j_\ell(kr_2)\; P(k|z_{12}) \,, \end{aligned} \tag{30}$$

so that in full sky $\sigma^2(z_1, z_2) = \sigma_0^2(z_1, z_2)$. Applying this to the SSC covariance of two observables, e.g. number counts, we have

$$\mathrm{Cov}^{\rm SSC}(\mathcal{O}_1, \mathcal{O}_2) = \frac{1}{f_{\rm SKY}^2} \sum_\ell \frac{2\ell+1}{4\pi}\, C_\ell(W)\, \mathrm{Cov}_\ell^{\rm SSC}(\mathcal{O}_1, \mathcal{O}_2) \,, \tag{31}$$

where

$$\begin{aligned} \mathrm{Cov}_\ell^{\rm SSC}(\mathcal{O}_1, \mathcal{O}_2) &= \int {\rm d}V_{12}\; \frac{\partial \mathfrak{o}_1}{\partial \delta_b}\; \frac{\partial \mathfrak{o}_1}{\partial \delta_b}\; \sigma_\ell^2(z_1, z_2) \\ &= \frac{1}{4\pi} \int {\rm d}V_{12}\; \frac{\partial \mathfrak{o}_1}{\partial \delta_b}\; \frac{\partial \mathfrak{o}_1}{\partial \delta_b}\; C_\ell^{\rm m}(z_1, z_2) \,. \end{aligned} \tag{32}$$

Therefore the combined Eqs. 29, 30, 31, 32, along with the window spectrum $C_\ell(W)$, allow for the computation of the SSC in partial sky for a general window and binning choice.

Numerically, we can pre-compute and tabulate $\mathrm{Cov}_\ell^{\rm SSC}(\mathcal{O}_1, \mathcal{O}_2)$, and then just change $C_\ell(W)$ as the mask varies. This enables easier studies of the mask effect such as optimisations of survey strategy (Takahashi et al. 2014), forecasts for improvements as a survey area grows, and comparisons between different surveys. Conversely, for a fixed survey with a well defined mask, we can pre-compute $C_\ell(W)$ for the specific survey mask, and change $\mathrm{Cov}_\ell^{\rm SSC}(\mathcal{O}_1, \mathcal{O}_2)$ as a function of cosmology within likelihood cosmological analyses, taking full account of geometry, mask, selection and cosmological dependencies in the covariances, and therefore deriving reliable parameter uncertainties.

4.3. Implementation

When estimating the SSC from Eq. 31, one numerical difficulty is the evaluation of the integral in Eq. 30, given that the Bessel functions highly oscillate with slow damping as $kr_i \to \infty$.

For the first multipoles, we may express the Bessel functions in terms of sine and cosine. Through trigonometrical identities, the integrals with products of Bessel function can thus be expressed as a sum of Fourier transforms. Derivations and expressions for the first 3 multipoles are given in Appendix C. For illustrative purposes we give below the expression for $\ell = 0$

$$C_0^{\rm m}(z_1, z_2) = \frac{I_0^c(r_1 - r_2) - I_0^c(r_1 + r_2)}{2} \,, \tag{33}$$

where

$$I_0^c(r) = \frac{2}{\pi} \int k^2\, {\rm d}k\; \cos(kr)\; P(k|z_{12})/k^2 \tag{34}$$

is a continuous cosine transform which can be efficiently approximated numerically with a discrete Fast Fourier Transform. However, as argued in Appendix C, this method becomes too cumbersome at high ℓ and may also become numerically unstable. We could carry it out only for $\ell = 0, 1, 2$.

As an alternative, we decided not to evaluate $\sigma^2(z_1, z_2)$, but instead to switch the order of the integrals over k and z, in order to compute directly the covariance as :

$$\begin{aligned} \mathrm{Cov}_\ell^{\rm SSC}(N_{\rm cl}(i_M, i_z), N_{\rm cl}(j_M, j_z)) = \frac{1}{2\pi^2} \int k^2 {\rm d}k\; P(k|z=0) \\ \times\; \Psi_\ell^{n_h}(k|i_M, i_z)\; \Psi_\ell^{n_h}(k|j_M, j_z) \,, \end{aligned} \tag{35}$$

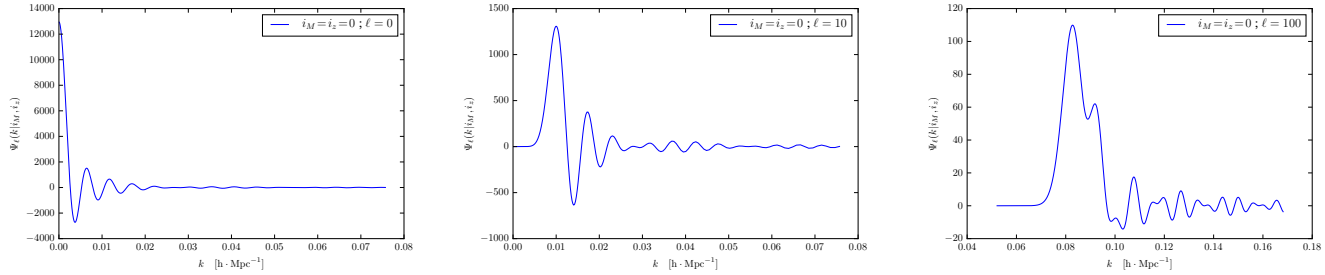

Fig. 3. $\Psi_\ell^{n_h}(k|i_M, i_z)$ as a function of k, for the representative case $i_M = i_z = 0$ ($\log M = 14 - 14.5$, $z = 0.4 - 0.5$). *Left:* at the lowest multipole $\ell = 0$. *Center:* at $\ell = 10$. *Right:* at $\ell = 100$.

where the kernel $\Psi_\ell^{n_h}$ is given by

$$\Psi_\ell^{n_h}(k|i_M, i_z) \equiv \int_{z\in\mathrm{bin}(i_z)} \mathrm{d}V\, G(z)\, \frac{\partial n_h}{\partial \delta_b}(i_M, z)\, j_\ell(kr)\,. \quad (36)$$

As can be seen in Fig. 3, this redshift integral effectively damps out the Bessel oscillations on scales $k > k_{\rm peak} + 2\pi/\Delta r(i_z)$ where $\Delta r(i_z) = r(z_{\rm max}) - r(z_{\rm min})$ is the width of the redshift bin in terms of comoving distance. This damping makes the k integral Eq. 35 much easier to deal with numerically compared to Eq. 25, since the integrand support is now more compact. This is the method we use for all numerical results shown hereafter in this article.

Alternatively, via the inversion of the $r(z)$ relation and defining a radial bin i_r from i_z, we note that Eq. 36 can be expressed as a Hankel transform

$$\Psi_\ell^{n_h}(k|i_M, i_r) = \int_{r\in\mathrm{bin}(i_r)} \mathrm{d}r\; r^2\, G(r)\, \frac{\partial n_h}{\partial \delta_b}(i_M, r)\, j_\ell(kr)\,, \quad (37)$$

which can be efficiently evaluated using Fast Fourier transform (FFT) methods such as FFTLog (e.g. Hamilton 2000; Camacho et al. in prep.).

Although the results presented in this article consider the case of cluster counts, the equations can be straightforwardly generalized to other probes of the large scale structure, see Appendix B.

5. Results

First, as a consistency test, we checked $\mathrm{Cov}_{\ell=0}^{\rm SSC}$ against the full sky covariance matrix computed via $\sigma^2_{\rm fullsky}(z_1, z_2)$ given in Eq. 9 (e.g. Lacasa & Rosenfeld 2016). We find good agreement, to 0.8% precision on the auto-redshift covariance, and 7% precision on the cross-redshift covariance.

Second, we show in Fig. 4 the general results for $\mathrm{Cov}_\ell^{\rm SSC}(N_{\rm cl}(i_M, i_z), N_{\rm cl}(j_M, j_z))$ in two representative cases: auto-covariance of the same redshift bin, and cross-covariance between two redshift bins. Both plots are for the lowest mass bin ($i_M = j_M = 0$, corresponding to $\log M = 14 - 14.5$), though the shape of the curves does not change when taking other mass bins (even with $i_M \neq j_M$), only their amplitude changes.

For the auto-covariance (left plot), we see that it first rises with ℓ, to a maximum corresponding to the angular scale of the matter-radiation equality (i.e. the peak of $P(k)$) at that redshift, and then decreases monotonically. This behaviour is conform to our expectations, since the scale dependence is that of a projection of the 3D power spectrum $P(k)$. It does mean that $C_\ell^m(z_1, z_2)$ is not constant with ℓ, and thus, as already discussed in Sect. 4, it means that the $f_{\rm SKY}$ approximation does not hold for super-sample covariance.

For the cross-covariance (right plot), the situation is interesting as we see that the covariance is first negative, the increases, crosses zero and reaches a maximum towards $\ell = 25$, then decreases asymptotically to zero. This means that small surveys will have a robustly negligible covariance between redshift bins (at least for this bin width $\Delta z = 0.1$), and can thus use block-diagonal covariance matrices to speed up their likelihoods estimations. However for surveys with a large sky coverage, the cross-covariance will be non-negligible and will depend on the survey area and shape, becoming either positive or negative depending on the mask. In those cases, careful estimation of the SSC is thus critical.

5.1. Application to a realistic survey mask

In order to illustrate the SSC method in a realistic case, we used two `Healpix` (Górski et al. 2005) masks visible in Fig. 5. The first one is a binary one and is broadly similar to the footprint of the Dark Energy Survey[6] (DES), though we warn that it does not in any way represent the actual DES survey area, and we do not attempt to draw any particular conclusion for that survey. This mask was created and kindly provided to us by Flavia Sobreira. The second mask represents a more pessimistic case, where we considered that 15% of the survey area had to be discarded due to bright stars, satellite trails, or other systematics. In order to simulate this effect, we simply upgraded the mask to high resolution (`nside`=4096), poked random holes in it, then degraded back the mask to the original resolution (`nside`=1024).

The angular power spectra $C_\ell(W)$ for these two masks can be seen on the left panel of Fig. 6. At low multipoles, the two spectra differ by a constant multiplicative factor 0.85^2, which is simply the ratio of the respective sky coverages. On smaller scales appear a second component in the spectrum of the second mask, which is a constant shot-noise due to the random holes. However we see that this component is very subdominant, hence we can already expect that the

[6] `www.darkenergysurvey.org`

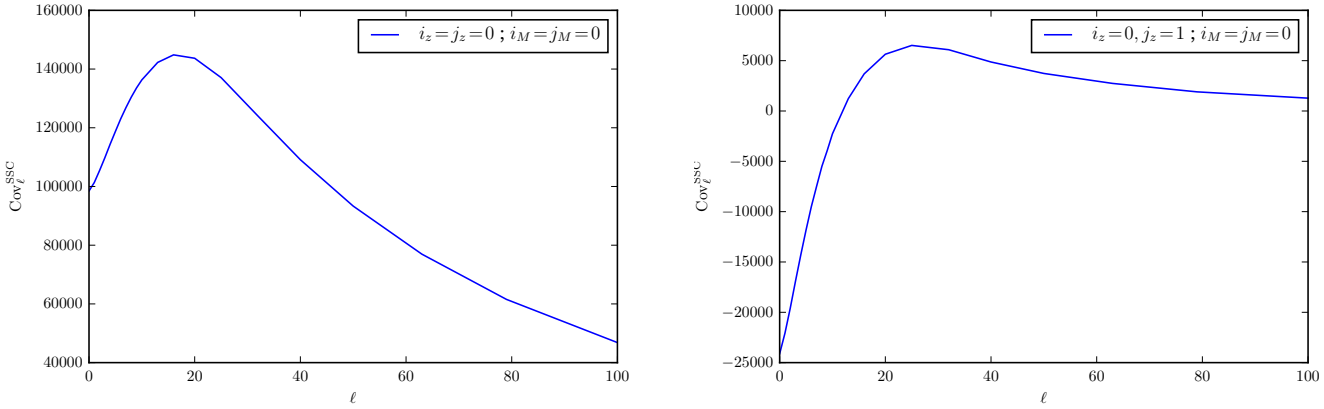

Fig. 4. $\mathrm{Cov}_\ell^{\mathrm{SSC}}$ as a function of ℓ, in the representative case $i_M = j_M = 0$ ($\log M = 14 - 14.5$). *Left:* same redshift $i_z = j_z = 0$ ($z = 0.4 - 0.5$). *Right:* cross-redshift $i_z = 1 \times j_z = 2$ ($z = [0.4 - 0.5] \times [0.5 - 0.6]$).

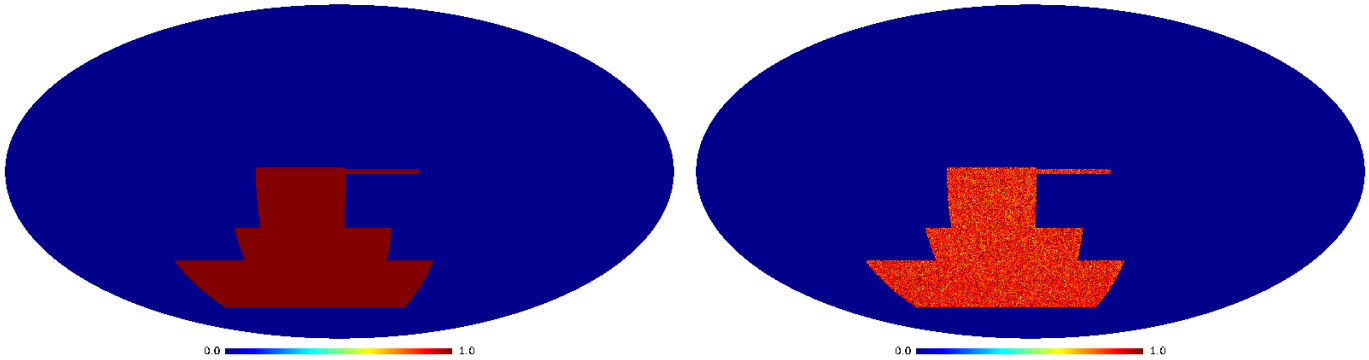

Fig. 5. Masks used in the analysis. *Left:* simple footprint, assumed observed uniformly. *Right:* same but with simulated 15% rejection of observations due to systematics (see text for details).

only difference between the covariance of the two masks will be due to the different sky coverage.

When implementing the sum over multipoles of Eq. 31, we find that we reached 1% convergence already at $\ell_{\mathrm{max}} = 50$. This means that $\mathrm{Cov}_\ell^{\mathrm{SSC}}$ need only be computed on a small number of multipoles for current and future surveys with large sky coverage, rendering the partial sky formalism developed here even more computationally efficient. Comparing the covariances of the two masks, we find that they indeed only differ due to the different sky fraction, but when renormalised by f_{SKY} they are identical to numerical precision (0.01% in our case). The corresponding correlation matrix is shown in the right of Fig. 6.

We see that SSC alone yields a near 100% correlation of all cluster counts in the same redshift bin. Concerning cross-redshifts, we find a ∼-15% anti-correlation between the adjacent bins. The cross-covariance is thus not negligible for such a large survey.

The formalism presented in Sect. 4 is thus perfectly adapted to the numerical prediction of super-sample covariance, even in the case of a complex survey geometry. In fact we see that such computation is indeed necessary, in order to reproduce the non-trivial behaviour of SSC, yielding e.g. non-negligible anti-correlation of redshift bins in the case presented above.

5.2. Flat sky limit

One remaining question is that of the link between the partial sky approach developed in Sect. 4, and the flat sky approximation used previously in the literature and shown in Eq. 10. The two approaches cannot be compared or related at the level of the formalism, because the $(k_\perp, k_\parallel)$ splitting does not apply for sufficiently large angles. However, we can compare what covariance the two formalism predict in some limits.

First, we can compare the equations analytically in the case of a constant spectrum $P(k|z_{12}) = \mathrm{cst} \equiv 1$. In the partial sky formalism we have:

$$C_\ell^m(z_1, z_2) = \frac{2}{\pi} \int k^2 \mathrm{d}k j_\ell(kr_1) j_\ell(kr_2) \times 1 = \frac{\delta(r_1 - r_2)}{r_1^2}\,, \tag{38}$$

and

$$\mathrm{Cov}_\ell^{\mathrm{SSC}}(N_{\mathrm{cl}}(i_M, i_z), N_{\mathrm{cl}}(j_M, j_z)) = \frac{\delta_{i_z, j_z}}{4\pi} \int \mathrm{d}V \, \frac{\partial n_h}{\partial \delta_b}(i_M, z) \, \frac{\partial n_h}{\partial \delta_b}(j_M, z) \tag{39}$$

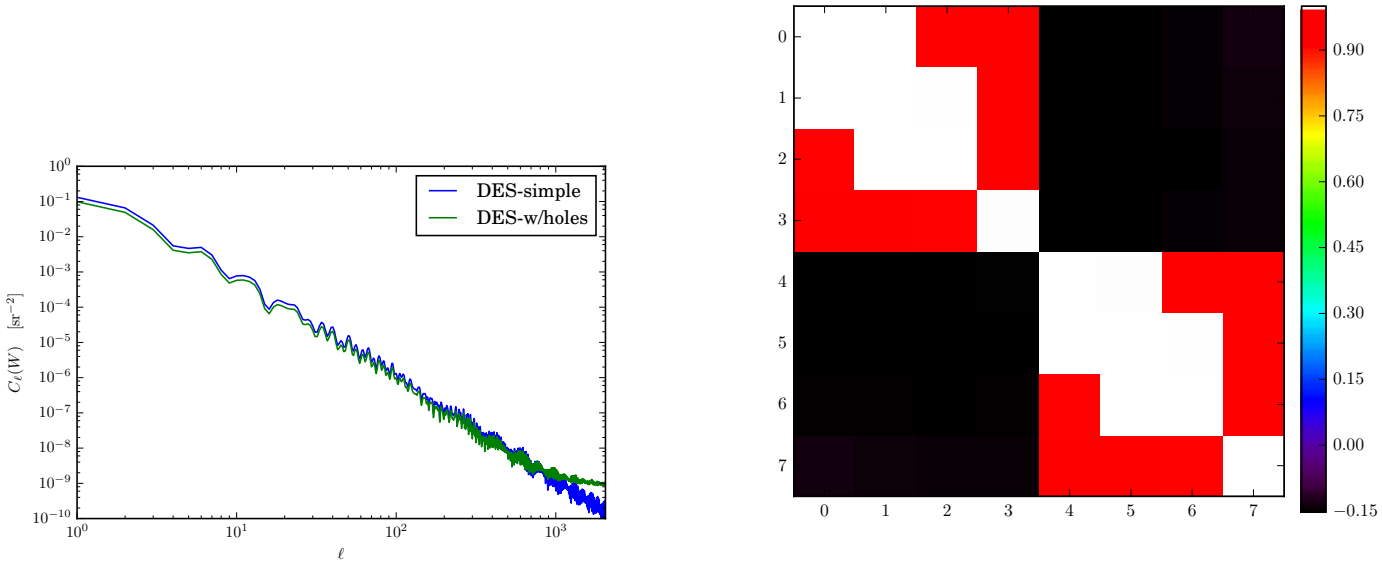

Fig. 6. *Left:* Angular power spectra of the two masks used in the analysis. *Right:* SSC correlation matrix (without shot-noise) of cluster counts for the first mask. White means 100% correlation, to 1 part in 255. The matrix is organized, as in Fig. 2, in two redshift blocks of increasing mass.

is independent of ℓ. Thus the SSC is given by

$$\begin{aligned}\mathrm{Cov}^{\mathrm{SSC}}(\cdots) &= \frac{\delta_{i_z,j_z}}{4\pi}\int \mathrm{d}V\,\frac{\partial n_h}{\partial\delta_b}(i_M,z)\,\frac{\partial n_h}{\partial\delta_b}(j_M,z)\\ &\quad\times\frac{1}{f_{\mathrm{SKY}}^2}\underbrace{\sum_\ell\frac{(2\ell+1)}{4\pi}C_\ell(W)}_{=f_{\mathrm{SKY}}}\\ &= \frac{\delta_{i_z,j_z}}{\Omega_S}\int \mathrm{d}V\,\frac{\partial n_h}{\partial\delta_b}(i_M,z)\,\frac{\partial n_h}{\partial\delta_b}(j_M,z)\,, \quad (40)\end{aligned}$$

where we made the counts N_{cl} implicit for the sake of clarity.

Now in the flat sky formalism we have:

$$\begin{aligned}\sigma^2(z_1,z_2) &= \frac{1}{2\pi^2}\int_0^\infty k_\perp\,\mathrm{d}k_\perp\,4\frac{J_1(k_\perp\theta_S r_1)}{k_\perp\theta_S r_1}\frac{J_1(k_\perp\theta_S r_2)}{k_\perp\theta_S r_2}\\ &\quad\times\underbrace{\int_0^\infty \mathrm{d}k_\parallel\,\cos\left[k_\parallel(r_1-r_2)\right]\times 1}_{=(2\pi)\,\delta(r_1-r_2)/2}\\ &= \frac{2}{\pi}\,\delta(r_1-r_2)\,\frac{1}{(\theta r_1)^2}\underbrace{\int x\,\mathrm{d}x\;\left(J_1(x)/x\right)^2}_{=1/2}\\ &= \frac{\delta(r_1-r_2)}{r_1^2}\times\frac{1}{\Omega_S}\,, \quad (41)\end{aligned}$$

where we changed variables $x = k_\perp\theta_S r_1$ and recall $\Omega_S \approx \pi\theta_S^2$. Inserting this into Eq. 7, we again obtain Eq. 40. Therefore the two approaches indeed agree in the flat sky limit for a constant spectrum.

Second, we can compare the results numerically for a mask with small enough sky coverage. To do so, we created a polar cap mask of radius 5 degree[7]. The power spectrum of this mask is shown in Fig. 7.

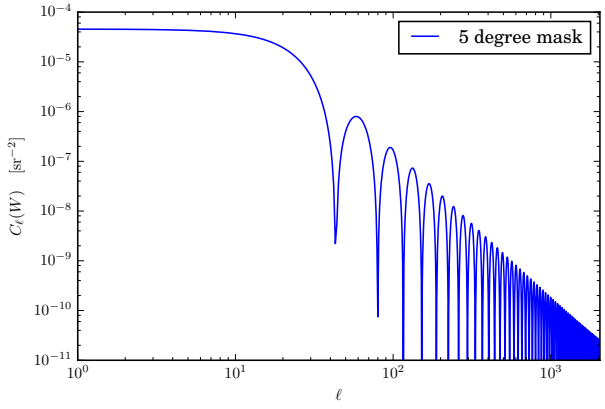

Fig. 7. Angular power spectrum of the 5 degree polar cap mask.

Compared to Fig. 6, here we see that power extends to smaller angular scales or higher multipoles. In this case, we found that we had to extend the sum in Eq. 31 to higher multipoles, $\ell_{\mathrm{max}} = 250$, in order to reach 1% level convergence of the covariance prediction. This stays however numerically tractable, through the observation that the ℓ dependence of $\mathrm{Cov}_\ell^{\mathrm{SSC}}$ is very smooth, especially after $\ell_{\mathrm{peak}} = 25$. Thus we can sample this dependence only for a small number of logarithmically-spaced multipoles, and interpolate when computing the sum in Eq. 31.

[7] As the power spectrum of a map is invariant under SO(3), centering the mask on the north pole is simply a convenient choice.

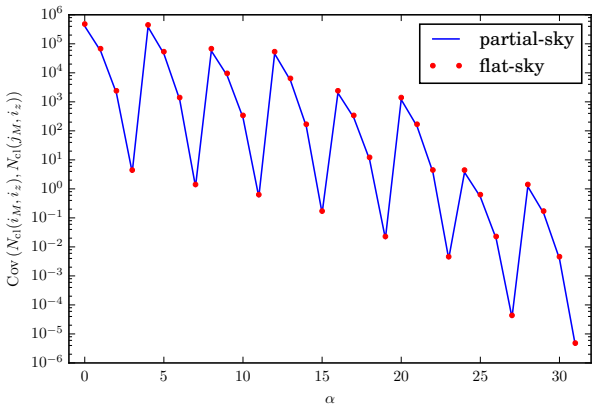

Fig. 8. Comparison of the SSC covariances derived from the partial sky formalism and the flat sky formula, for a 5 deg circular sky patch. Auto-z covariances are shown as a function of $\alpha = j_M + n_M\, i_M + n_M^2\, i_z$ (see text for details).

We found good agreement between the covariance derived from the partial sky formalism, and that derived from the flat sky limit Eq. 10. This is visible e.g. in Fig. 8 showing both auto-z covariances as a function of $\alpha = j_M + n_M\, i_M + n_M^2\, i_z$, i.e. the first four points show the covariance for $i_M = i_z = 0$ and varying j_M, etc. This order is simply a convenient one to plot this multi-variable function.

The partial sky formalism thus successfully recovers the flat sky approximation in the flat sky limit. Numerically, we even found the partial sky formalism to be faster than the full computation of Eq. 10, and only 3 times slower than the Sij approximation Eq. 11.

6. Conclusion

Super-sample covariance, also often called sample variance, is the dominant error for cluster counts at low cluster masses. For instance, Hu & Cohn (2006) have shown that even for a survey radius $\theta = 2.4$ deg, the sample covariance is of the same order of magnitude as shot noise for cluster counts above $\log M = 14.2$, though shot noise dominates for a threshold $\log M = 14.4$. As shot-noise decreases faster with survey area than SSC, careful predictions of SSC become crucial for current and future surveys covering ever larger sky areas. It becomes even more crucial as these surveys will be able to probe lower cluster masses, through a higher density of galaxy detections. SSC is also crucial to the analysis of galaxy clustering and lensing shear, where it dominates statistical errors on small scales, and for probe combinations as it has been shown to couple probes together (Takada & Bridle 2007; Takada & Spergel 2014; Lacasa & Rosenfeld 2016).

In the case of cluster counts covariance, we examined theoretical SSC computations methods in the flat sky limit, comparing two analytical approximations proposed in the literature to a full computation. We found that both approximations underpredict the auto-z covariance by 15% to 30-35%.

We then presented a harmonic expansion method for efficiently and accurately computing SSC for an arbitrary survey window function. We developed the method in the case of cluster counts, but it can be straightforwardly generalized to other probes such as galaxy clustering or lensing shear. Our derived expressions generalize previous full sky and flat sky equations found in the literature, properly reducing to them in the corresponding limits. We have cast the final covariance expression from the partial sky formalism in a way that allows easy modification of the survey mask. This is particularly suitable for comparison of surveys, design of survey strategy, as well as tests of data cuts due to quality selection criteria or systematics.

When applying our partial sky formalism to a mask broadly similar to the Dark Energy Survey footprint with $f_{\rm SKY} \sim 10\%$, we found a $\sim -15\%$ cross-z covariance, meaning that the observables in the two redshift bins considered are anti-correlated. Hence the covariance matrix cannot be taken as block diagonal, as is the case for the approximation by Krause & Eifler (2016) (which is however restricted to the flat sky limit). We also examined the possibility that the survey area is further reduced by pixel removal due e.g. to bright stars or systematics. We found that this does not have important effects on the structure of the SSC matrix, only re-scaling its amplitude by the effective survey area.

The results presented in this article thus render possible the theoretical computation of LSS covariances that account for selection and mask effect and also vary as a function of model parameters, as is the case in e.g. CMB analyses. The latter parameter dependence is important in the case of likelihood analysis of cluster constraints, as it allows for self-calibration of the cluster observable-mass relation (Lima & Hu 2005; Hu & Cohn 2006; Baxter et al. 2016). For general probes, it can also improve cosmological parameter constraints from likelihood inference analyses compared to methods that either neglect these effects or fix the covariance from data or simulations, avoiding e.g. the risk of fixing the covariance at a potentially incorrect cosmology. In future work, we plan to examine the relation between these theoretical predictions with covariances estimated from data itself (subsampling, jackknife and bootstrap methods) as well as from simulations.

Acknowledgements

We thank Flavia Sobreira for providing us with a mask of a DES-like survey footprint. We acknowledge the use of the `Healpix` package by Górski et al. (2005). FL acknowledges support by the Swiss National Science Foundation. ML is partially supported by FAPESP and CNPq. MA is supported by FAPESP.

References

Aguena, M. & Lima, M. 2016, ArXiv e-prints [arXiv:1611.05468]
Astier, P., Guy, J., Regnault, N., et al. 2006, Astronomy and Astrophysics, 447, 31
Baxter, E. J., Rozo, E., Jain, B., Rykoff, E., & Wechsler, R. H. 2016, MNRAS, 463, 205
Bayliss, M. B., Ruel, J., Stubbs, C. W., et al. 2016, ApJS, 227, 3
Beutler, F., Seo, H.-J., Ross, A. J., et al. 2017, MNRAS, 464, 3409
Bleem, L. E., Stalder, B., de Haan, T., et al. 2015, ApJS, 216, 27
Blot, L., Corasaniti, P. S., Amendola, L., & Kitching, T. D. 2016, MNRAS, 458, 4462
Camacho, H. et al. in prep.
Cooray, A. & Sheth, R. 2002, Phys. Rep., 372, 1
Crocce, M., Carretero, J., Bauer, A. H., et al. 2016, MNRAS, 455, 4301

Dietrich, J. P., Zhang, Y., Song, J., et al. 2014, MNRAS, 443, 1713
Dodelson, S. & Schneider, M. D. 2013, Phys. Rev. D, 88, 063537
Eisenstein, D. J. & Hu, W. 1998, ApJ, 496, 605
Escoffier, S., Cousinou, M.-C., Tilquin, A., et al. 2016, ArXiv e-prints [arXiv:1606.00233]
Giannantonio, T., Fosalba, P., Cawthon, R., et al. 2016, MNRAS, 456, 3213
Górski, K. M., Hivon, E., Banday, A. J., et al. 2005, ApJ, 622, 759
Hamilton, A. J. S. 2000, MNRAS, 312, 257
Hildebrandt, H., Viola, M., Heymans, C., et al. 2016, ArXiv e-prints [arXiv:1606.05338]
Hinton, S. R., Kazin, E., Davis, T. M., et al. 2017, MNRAS, 464, 4807
Hivon, E., Górski, K. M., Netterfield, C. B., et al. 2002, ApJ, 567, 2
Hu, W., Chiang, C.-T., Li, Y., & LoVerde, M. 2016, ArXiv e-prints [arXiv:1605.01412]
Hu, W. & Cohn, J. D. 2006, Phys. Rev. D, 73, 067301
Hu, W. & Kravtsov, A. V. 2003, ApJ, 584, 702
Koester, B. P., McKay, T. A., Annis, J., et al. 2007, ApJ, 660, 221
Krause, E. & Eifler, T. 2016, ArXiv e-prints [arXiv:1601.05779]
Lacasa, F. & Rosenfeld, R. 2016, J. Cosmology Astropart. Phys., 8, 005
Li, Y., Hu, W., & Takada, M. 2014a, Phys. Rev. D, 89, 083519
Li, Y., Hu, W., & Takada, M. 2014b, Phys. Rev. D, 90, 103530
Li, Y., Hu, W., & Takada, M. 2016, Phys. Rev. D, 93, 063507
Lima, M. & Hu, W. 2004, Phys. Rev. D, 70, 043504
Lima, M. & Hu, W. 2005, Phys. Rev. D, 72, 043006
Lima, M. & Hu, W. 2007, Phys. Rev. D, 76, 123013
Miller, C. J., Nichol, R. C., Reichart, D., et al. 2005, AJ, 130, 968
O'Connell, R., Eisenstein, D., Vargas, M., Ho, S., & Padmanabhan, N. 2016, MNRAS, 462, 2681
Pearson, D. W. & Samushia, L. 2016, MNRAS, 457, 993
Peebles, P. J. E. 1980, The large-scale structure of the universe
Percival, W. J., Reid, B. A., Eisenstein, D. J., & et al. 2010, Monthly Notices of the Royal Astronomical Society, 401, 2148
Planck Collaboration, Ade, P. A. R., Aghanim, N., et al. 2016, A&A, 594, A27
Riess, A. G., Macri, L., Casertano, S., et al. 2009, The Astrophysical Journal, 699, 539
Rykoff, E. S., Rozo, E., Busha, M. T., et al. 2014, ApJ, 785, 104
Rykoff, E. S., Rozo, E., Hollowood, D., et al. 2016, ApJS, 224, 1
Sánchez, C., Carrasco Kind, M., Lin, H., et al. 2014, MNRAS, 445, 1482
Schmidt, F., Jeong, D., & Desjacques, V. 2013, Phys. Rev. D, 88, 023515
Schmidt, F., Lima, M., Oyaizu, H., & Hu, W. 2009, Phys. Rev. D, 79, 083518
Shirasaki, M., Takada, M., Miyatake, H., et al. 2016, ArXiv e-prints [arXiv:1607.08679]
Singh, S., Mandelbaum, R., Seljak, U., Slosar, A., & Vazquez Gonzalez, J. 2016, ArXiv e-prints [arXiv:1611.00752]
Soares-Santos, M., de Carvalho, R. R., Annis, J., et al. 2011, ApJ, 727, 45
Takada, M. & Bridle, S. 2007, New Journal of Physics, 9, 446
Takada, M. & Hu, W. 2013, Phys. Rev. D, 87, 123504
Takada, M. & Spergel, D. N. 2014, MNRAS, 441, 2456
Takahashi, R., Soma, S., Takada, M., & Kayo, I. 2014, MNRAS, 444, 3473
Tinker, J., Kravtsov, A. V., Klypin, A., et al. 2008, ApJ, 688, 709
Tinker, J. L., Robertson, B. E., Kravtsov, A. V., et al. 2010, ApJ, 724, 878

Appendix A: Redshift-dependent mask

In the case where the survey angular mask W depends on redshift (e.g. when there are significant depth variations in the sky), the definition of the background mode Eq. 3 is simply changed to

$$\delta_b(z) = \frac{1}{\Omega_S(z)} \int \mathrm{d}^2\hat{\mathbf{n}}\; W(\hat{\mathbf{n}}, z)\; \delta(r\hat{\mathbf{n}}, z)\,, \tag{A.1}$$

where now the survey solid angle Ω_S depends on redshift.

Then Eq. 24 for $\sigma^2(z_1, z_2)$ is changed to

$$\sigma^2(z_1, z_2) = \frac{1}{\Omega_S(z_1)\,\Omega_S(z_2)} \sum_\ell \{\; (2\ell+1)\; C_\ell[W(z_1), W(z_2)] \times C_\ell^m(z_1, z_2)\; \}\,, \tag{A.2}$$

where $C_\ell[W(z_1), W(z_2)]$ is the angular cross-spectrum between the two masks at the two redshifts. This equation can then be integrated over (z_1, z_2) through Eq. 4 to yield the SSC covariance.

We note that in this redshift-dependent case, we can no longer permute the k and z integrals as was done in Sect. 4.3, which yielded a numerically efficient method. Finding an equally efficient method to compute the SSC in the general case of redshift-dependent angular window and partial sky coverage remains, to the best of our knowledge, as an important open problem.

Appendix B: SSC for other probes

The main results of this article were derived for the covariance of cluster number counts. However, it is straightforward to generalise the equations to other large scale structure probes, such as galaxy clustering and lensing shear. In those cases, the covariance equations are simpler for the angular power spectrum C_ℓ than for the angular correlation function. For instance, using Limber's approximation, Lacasa & Rosenfeld (2016) have shown that the SSC of the galaxy angular power spectrum is given by:

$$\mathrm{Cov}\left(C_{\ell_1}^{\mathrm{gal}}(i_z), C_{\ell_2}^{\mathrm{gal}}(j_z)\right) = \int \mathrm{d}V_{12}\; \frac{\overline{n}_{\mathrm{gal}}(z_1)\,\overline{n}_{\mathrm{gal}}(z_2)}{\Delta N_{\mathrm{gal}}(i_z)\,\Delta N_{\mathrm{gal}}(j_z)} \times \frac{\partial P_{\mathrm{gal}}(k_{\ell_1}, z_1)}{\partial \delta_b}\; \frac{\partial P_{\mathrm{gal}}(k_{\ell_2}, z_2)}{\partial \delta_b} \times \sigma^2(z_1, z_2)\,, \tag{B.1}$$

where $k_{\ell_i} = (\ell_i + 1/2)/r(z_i)$.

For lensing shear, we would get a similar equation, replacing the galaxy number density by the lensing selection function and the 3D galaxy power spectrum by the matter power spectrum. The equation can thus be generalized to

$$\mathrm{Cov}\left(C_{\ell_1}^{\alpha}(i_z), C_{\ell_2}^{\alpha}(j_z)\right) = \int \mathrm{d}V_{12}\; W_\alpha(z_1)\, W_\alpha(z_2) \times \frac{\partial P_\alpha(k_{\ell_1}, z_1)}{\partial \delta_b}\; \frac{\partial P_\alpha(k_{\ell_2}, z_2)}{\partial \delta_b} \times \sigma^2(z_1, z_2)\,, \tag{B.2}$$

where the α index refers to either lensing or galaxy, and W_α is the corresponding selection function. In that case, it is straightforward to generalize Eq. 35, even including the possibility of the cross-covariance between galaxy and shear:

$$\mathrm{Cov}_\ell\left(C_{\ell_1}^{\alpha}(i_z), C_{\ell_2}^{\beta}(j_z)\right) = \frac{1}{2\pi^2} \int k^2\,\mathrm{d}k\; P(k|z=0) \times \Psi_\ell^{\ell_1,\alpha}(k|i_z)\; \Psi_\ell^{\ell_2,\beta}(k|j_z)\,, \tag{B.3}$$

where

$$\Psi_\ell^{\ell_i,\alpha}(k|i_z) \equiv \int_{z\in\mathrm{bin}(i_z)} \mathrm{d}V\; G(z)\, W_\alpha(z)\, \frac{\partial P_\alpha(k_{\ell_i}, z)}{\partial \delta_b}\, j_\ell(kr)\,. \tag{B.4}$$

And the cross-covariance between cluster counts and either galaxy or shear:

$$\mathrm{Cov}_\ell\left(N_{\mathrm{cl}}(i_M, i_z), C_{\ell_2}^{\beta}(j_z)\right) = \frac{1}{2\pi^2} \int k^2\,\mathrm{d}k\; P(k|z=0) \times \Psi_\ell^{n_h}(k|i_M, i_z)\, \Psi_\ell^{\ell_2,\beta}(k|j_z)\,, \tag{B.5}$$

which gives us all the equations needed to compute the auto and cross-covariances of cluster counts, galaxy angular power spectrum, and lensing shear power spectrum, i.e. the three main cosmological probes of current and future photometric galaxy surveys.

Appendix C: First multipoles

The spherical Bessel functions $j_n(x)$ obey the recurrence relation

$$j_{n+1}(x) = \frac{2n+1}{x} j_n(x) - j_{n-1}(x)\,, \tag{C.1}$$

such that they can be written analytically in terms of sines, cosines and polynomials, given the initial conditions

$$j_{-1}(x) = \frac{\cos(x)}{x}\,, \tag{C.2}$$

$$j_0(x) = \frac{\sin(x)}{x}\,. \tag{C.3}$$

The first few spherical Bessel functions are given by

$$j_0(x) = \frac{\sin(x)}{x}\,, \tag{C.4}$$

$$j_1(x) = \frac{1}{x}\frac{\sin(x)}{x} - \frac{\cos(x)}{x}\,, \tag{C.5}$$

$$j_2(x) = \left(\frac{3}{x^2} - 1\right)\frac{\sin(x)}{x} - \frac{3}{x}\frac{\cos(x)}{x}\,. \tag{C.6}$$

Recall that we are trying to compute the following integrals :

$$C_\ell^{\rm m}(z_{12}) = \frac{2}{\pi}\int k^2{\rm d}k\; j_\ell(kr_1)\, j_\ell(kr_2)\; P(k|z_{12})\,. \tag{C.7}$$

For $j_\ell(x)$ of the form $A_\ell(x)\sin(x)/x - B_\ell(x)\cos(x)/x$, this yields

$$\begin{aligned} C_\ell^{\rm m}(z_{12}) = \frac{2}{\pi}\int k^2{\rm d}k\; \frac{P(k|z_{12})}{k^2 r_1 r_2} \\ \times \frac{1}{2}\Big[\big(A_\ell(kr_1)A_\ell(kr_2) + B_\ell(kr_1)B_\ell(kr_2)\big) \\ \times\cos\big(k(r_1-r_2)\big) \\ +\big(-A_\ell(kr_1)A_\ell(kr_2) + B_\ell(kr_1)B_\ell(kr_2)\big) \\ \times\cos\big(k(r_1+r_2)\big) \\ -\big(A_\ell(kr_1)B_\ell(kr_2) - B_\ell(kr_1)A_\ell(kr_2)\big) \\ \times\sin\big(k(r_1-r_2)\big) \\ -\big(A_\ell(kr_1)B_\ell(kr_2) + B_\ell(kr_1)A_\ell(kr_2)\big) \\ \times\sin\big(k(r_1+r_2)\big)\Big]\,, \end{aligned} \tag{C.8}$$

where the four integrals are Fourier (sine/cosine) transforms and can be computed numerically with FFTs. Let us note

$$\begin{aligned} I_c^+\big(f(k,r_1,r_2)\big) \equiv \frac{2}{\pi}\int k^2{\rm d}k\; \frac{P(k|z_{12})}{k^2 r_1 r_2}\; f(k,r_1,r_2) \\ \times\cos\big(k(r_1+r_2)\big)\,, \end{aligned} \tag{C.9}$$

$$\begin{aligned} I_c^-\big(f(k,r_1,r_2)\big) \equiv \frac{2}{\pi}\int k^2{\rm d}k\; \frac{P(k|z_{12})}{k^2 r_1 r_2}\; f(k,r_1,r_2) \\ \times\cos\big(k(r_1-r_2)\big)\,, \end{aligned} \tag{C.10}$$

$$\begin{aligned} I_s^+\big(f(k,r_1,r_2)\big) \equiv \frac{2}{\pi}\int k^2{\rm d}k\; \frac{P(k|z_{12})}{k^2 r_1 r_2}\; f(k,r_1,r_2) \\ \times\sin\big(k(r_1+r_2)\big)\,, \end{aligned} \tag{C.11}$$

$$\begin{aligned} I_s^-\big(f(k,r_1,r_2)\big) \equiv \frac{2}{\pi}\int k^2{\rm d}k\; \frac{P(k|z_{12})}{k^2 r_1 r_2}\; f(k,r_1,r_2) \\ \times\sin\big(k(r_1-r_2)\big)\,. \end{aligned} \tag{C.12}$$

Then Eq. C.8 can be rewritten as

$$\begin{aligned} C_\ell^{\rm m}(z_{12}) = \frac{1}{2}\Big[&I_c^-\big(A_{\ell,1}A_{\ell,2} + B_{\ell,1}B_{\ell,2}\big) \\ &+ I_c^+\big(-A_{\ell,1}A_{\ell,2} + B_{\ell,1}B_{\ell,2}\big) \\ &- I_s^-\big(A_{\ell,1}B_{\ell,2} - B_{\ell,1}A_{\ell,2}\big) \\ &- I_s^+\big(A_{\ell,1}B_{\ell,2} + B_{\ell,1}A_{\ell,2}\big)\Big]\,, \end{aligned} \tag{C.13}$$

with $A_{\ell,i} = A_\ell(kr_i)$. For $\ell = 0$ we have $A_0 = 1$ and $B_0 = 0$, thus

$$C_0^{\rm m}(z_{12}) = \frac{1}{2}\left[I_c^-(1) - I_c^+(1)\right]. \tag{C.14}$$

For $\ell = 1$ we have $A_1 = 1/x$ and $B_1 = 1$. Therefore

$$\begin{aligned} C_1^{\rm m}(z_{12}) = \frac{1}{2}\Bigg[&I_c^-\left(\frac{1}{k^2 r_1 r_2} + 1\right) + I_c^+\left(-\frac{1}{k^2 r_1 r_2} + 1\right) \\ &- I_s^-\left(\frac{1}{kr_1} - \frac{1}{kr_2}\right) - I_s^+\left(\frac{1}{kr_1} + \frac{1}{kr_2}\right)\Bigg]\,. \end{aligned} \tag{C.15}$$

If we define $I_{c/s,n}^{+/-} \equiv I_{c/s}^{+/-}(1/k^n)$, the above equations yield

$$C_0^{\rm m}(z_{12}) = \frac{1}{2}\left[I_{c,0}^- - I_{c,0}^+\right], \tag{C.16}$$

$$\begin{aligned} C_1^{\rm m}(z_{12}) = \frac{1}{2}\Bigg[&I_{c,0}^- + I_{c,0}^+ - I_{s,1}^-\left(\frac{1}{r_1} - \frac{1}{r_2}\right) \\ &- I_{s,1}^+\left(\frac{1}{r_1} + \frac{1}{r_2}\right) + \frac{I_{c,2}^- - I_{c,2}^+}{r_1 r_2}\Bigg]\,, \end{aligned} \tag{C.17}$$

For $\ell = 2$ we have $A_2 = 3/x^2 - 1$ and $B_2 = 3/x$, thus

$$\begin{aligned} C_2^{\rm m}(z_{12}) = \frac{1}{2}\Bigg[& I_c^- \left(\frac{9}{k^4 r_1^2 r_2^2} + \frac{3}{k^2}\left(\frac{3}{r_1 r_2} - \frac{1}{r_1^2} - \frac{1}{r_2^2} \right) + 1 \right) \\ & + I_c^+ \left(-\frac{9}{k^4 r_1^2 r_2^2} + \frac{3}{k^2}\left(\frac{3}{r_1 r_2} + \frac{1}{r_1^2} + \frac{1}{r_2^2} \right) - 1 \right) \\ & - I_s^- \left(\frac{9}{k^3 r_1 r_2} + \frac{3}{k} \right) \times \left(\frac{1}{r_1} - \frac{1}{r_2} \right) \\ & - I_s^+ \left(\frac{9}{k^3 r_1 r_2} - \frac{3}{k} \right) \times \left(\frac{1}{r_1} + \frac{1}{r_2} \right) \Bigg] \qquad \text{(C.18)} \\ = \frac{1}{2}\Bigg[& I_{c,0}^- - I_{c,0}^+ - 3\, I_{s,1}^- \left(\frac{1}{r_1} - \frac{1}{r_2} \right) \\ & + 3\, I_{s,1}^+ \left(\frac{1}{r_1} + \frac{1}{r_2} \right) + 3\, I_{c,2}^- \left(\frac{3}{r_1 r_2} - \frac{1}{r_1^2} - \frac{1}{r_2^2} \right) \\ & + 3\, I_{c,2}^+ \left(\frac{3}{r_1 r_2} + \frac{1}{r_1^2} + \frac{1}{r_2^2} \right) - \frac{9\, I_{s,3}^-}{r_1 r_2} \left(\frac{1}{r_1} - \frac{1}{r_2} \right) \\ & - \frac{9\, I_{s,3}^+}{r_1 r_2} \left(\frac{1}{r_1} + \frac{1}{r_2} \right) + \frac{9\left(I_{c,4}^- - I_{c,4}^+ \right)}{r_1^2 r_2^2} \Bigg] . \qquad \text{(C.19)} \end{aligned}$$

We note that A_ℓ and B_ℓ follow the same recurrence relation Eq. C.1 as the spherical Bessel functions j_n. As such we can look whether there is a recurrence relation which would allow us to get the analytical formula for a general $C_\ell^{\rm m}(z_{12})$. Our efforts in this direction have shown only partially fruitful and are described below. We have

$$\begin{aligned} C_{\ell+1}^{\rm m}(z_{12}) = \frac{1}{2}\Big[& I_c^-\big(A_{\ell+1,1}A_{\ell+1,2} + B_{\ell+1,1}B_{\ell+1,2} \big) \\ & + I_c^+\big(-A_{\ell+1,1}A_{\ell+1,2} + B_{\ell+1,1}B_{\ell+1,2} \big) \\ & - I_s^-\big(A_{\ell+1,1}B_{\ell+1,2} - B_{\ell+1,1}A_{\ell+1,2} \big) \\ & - I_s^+\big(A_{\ell+1,1}B_{\ell+1,2} + B_{\ell+1,1}A_{\ell+1,2} \big) \Big] \\ \equiv \frac{1}{2}\left(C_{\ell+1}^{c,-} + C_{\ell+1}^{c,+} - C_{\ell+1}^{s,-} - C_{\ell+1}^{s,+} \right) , & \qquad \text{(C.20)} \end{aligned}$$

and then

$$\begin{aligned} C_{\ell+1}^{c,-} = & I_c^- \Bigg[\left(\frac{2\ell+1}{kr_1} A_{\ell,1} - A_{\ell-1,1} \right) \left(\frac{2\ell+1}{kr_2} A_{\ell,2} - A_{\ell-1,2} \right) \\ & + \left(\frac{2\ell+1}{kr_1} B_{\ell,1} - B_{\ell-1,1} \right) \left(\frac{2\ell+1}{kr_2} B_{\ell,2} - B_{\ell-1,2} \right) \Bigg] \qquad \text{(C.21)} \\ = & \, C_{\ell-1}^{c,-} + \frac{(2\ell+1)^2}{r_1 r_2} I_c^-\left[\left(A_{\ell,1}A_{\ell,2} + B_{\ell,1}B_{\ell,2} \right)/k^2 \right] \\ & - (2\ell+1)\, I_c^-\big[(A_{\ell-1,1}A_{\ell,2} + B_{\ell-1,1}B_{\ell,2})/kr_1 \\ & \qquad + (1 \leftrightarrow 2) \big] . \qquad \text{(C.22)} \end{aligned}$$

Now we define the following quantities

$$D_\ell^{c,-} \equiv I_c^-\left[(A_{\ell-1,1}A_{\ell,2} + B_{\ell-1,1}B_{\ell,2})/kr_1 + (1 \leftrightarrow 2) \right] , \qquad \text{(C.23)}$$

$$E_\ell^{c,-} \equiv I_c^-\left[(A_{\ell-1,1}A_{\ell,2} + B_{\ell-1,1}B_{\ell,2})/kr_2 + (1 \leftrightarrow 2) \right] , \qquad \text{(C.24)}$$

and decompose $C_\ell^{c,-}$, $D_\ell^{c,-}$ and $E_\ell^{c,-}$ onto the basis $I_{c,i}^-$

$$C_\ell^{c,-} = \sum_{i=0}^{+\infty} \alpha_{\ell,i}^{c,-}(r_1, r_2) I_{c,i}^- , \qquad \text{(C.25)}$$

$$D_\ell^{c,-} = \sum_{i=0}^{+\infty} \beta_{\ell,i}^{c,-}(r_1, r_2) I_{c,i}^- , \qquad \text{(C.26)}$$

$$E_\ell^{c,-} = \sum_{i=0}^{+\infty} \gamma_{\ell,i}^{c,-}(r_1, r_2) I_{c,i}^- . \qquad \text{(C.27)}$$

Then Eq. C.22 gives a first recurrence relation

$$\alpha_{\ell+1,i}^{c,-} = \alpha_{\ell-1,i}^{c,-} + \frac{(2\ell+1)^2}{r_1 r_2} \alpha_{\ell,i-2}^{c,-} - (2\ell+1)\beta_{\ell,i}^{c,-} . \qquad \text{(C.28)}$$

By computing $D_{\ell+1}^{c,-}$ and $E_{\ell+1}^{c,-}$, we can see that we have the two other recurrence relations :

$$\beta_{\ell+1,i}^{c,-} = (2\ell+1)\frac{2}{r_1 r_2} \alpha_{\ell,i-2}^{c,-} - \gamma_{\ell,i}^{c,-} , \qquad \text{(C.29)}$$

$$\gamma_{\ell+1,i}^{c,-} = (2\ell+1)\left(\frac{1}{r_1^2} + \frac{1}{r_2^2} \right) \alpha_{\ell,i-2}^{c,-} - \beta_{\ell,i}^{c,-} . \qquad \text{(C.30)}$$

The system is closed through the initial conditions

$$\alpha_{0,0}^{c,-} = 1 \quad \alpha_{0,2}^{c,-} = 0 \qquad \alpha_{0,i}^{c,-} = 0 \text{ for } i \geq 3 \qquad \text{(C.31)}$$

$$\alpha_{1,0}^{c,-} = 1 \quad \alpha_{1,2}^{c,-} = \frac{1}{r_1 r_2} \qquad \alpha_{1,i}^{c,-} = 0 \text{ for } i \geq 3 \qquad \text{(C.32)}$$

$$\beta_{1,0}^{c,-} = 0 \quad \beta_{1,2}^{c,-} = \frac{2}{r_1 r_2} \qquad \beta_{1,i}^{c,-} = 0 \text{ for } i \geq 3 \qquad \text{(C.33)}$$

$$\gamma_{1,0}^{c,-} = 0 \quad \gamma_{1,2}^{c,-} = \left(\frac{1}{r_1^2} + \frac{1}{r_2^2} \right) \quad \gamma_{1,i}^{c,-} = 0 \text{ for } i \geq 3 \qquad \text{(C.34)}$$

The following properties can easily be shown by recurrence:

$$\forall \ell \qquad \alpha_{\ell,0}^{c,-} = 1 , \qquad \beta_{\ell,0}^{c,-} = 0 , \qquad \gamma_{\ell,0}^{c,-} = 0 . \qquad \text{(C.35)}$$

$$\forall \ell \qquad \alpha_{\ell,i}^{c,-} = 0 , \qquad \text{if } i \text{ odd or } i > 2\ell . \qquad \text{(C.36)}$$

$$\forall \ell \qquad \alpha_{\ell,2\ell}^{c,-} = \frac{\prod_{n=0}^{\ell-1}(2n+1)^2}{(r_1 r_2)^\ell} = \frac{(2\ell-1)!^2}{(4 r_1 r_2)^\ell\, \ell!^2} . \qquad \text{(C.37)}$$

With a bit more work, we can in principle solve for $\beta_{\ell,2}^{c,-}$ and $\gamma_{\ell,2}^{c,-}$, since $\alpha_{\ell,0}^{c,-} = 1$:

$$\beta_{\ell+1,2}^{c,-} = (2\ell+1)\frac{2}{r_1 r_2} - \gamma_{\ell,2}^{c,-} , \qquad \text{(C.38)}$$

$$\gamma_{\ell+1,2}^{c,-} = (2\ell+1)\left(\frac{1}{r_1^2} + \frac{1}{r_2^2} \right) - \beta_{\ell,2}^{c,-} . \qquad \text{(C.39)}$$

This can be put in the form

$$X_{\ell+1} = M X_\ell + V_\ell , \qquad \text{(C.40)}$$

for

$$X_\ell = \begin{pmatrix} \beta_{\ell,2}^{c,-} \\ \gamma_{\ell,2}^{c,-} \end{pmatrix} , \qquad \text{(C.41)}$$

$$M = \begin{pmatrix} 0 & -1 \\ -1 & 0 \end{pmatrix} , \qquad \text{(C.42)}$$

$$V_\ell = (2\ell+1)\begin{pmatrix} \frac{2}{r_1 r_2} \\ \frac{1}{r_1^2} + \frac{1}{r_2^2} \end{pmatrix} = (2\ell+1) X_1 . \qquad \text{(C.43)}$$

Finally, Eq. C.40 has the following solution :

$$X_\ell = \sum_{k=0}^{\ell-1} M^{\ell-k-1}\ (2k+1) X_1\,, \tag{C.44}$$

which in principle gives the solution for $\beta^{c,-}_{\ell,2}$ and $\gamma^{c,-}_{\ell,2}$. We can insert this into Eq. C.28 for $i = 2$, to get a closed recurrence relation for $\alpha^{c,-}_{\ell,2}$ and solve for it. In turn, this can be inserted into Eqs. C.29 and C.30 for $i = 4$ to get a closed recurrence relation for $(\beta^{c,-}_{\ell,4}, \gamma^{c,-}_{\ell,4})$, and so on. So this represents a procedure for solving this set of equations and get analytical expressions for $C_\ell^{c,-}$. Similarly, we could derive recurrence relations for $C_\ell^{c,+}$, $C_\ell^{s,-}$ and $C_\ell^{s,+}$. In practice this represents a daunting task, as even the formula for $\ell = 2$ (Eq. C.19) is already cumbersome.

Moreover, we may expect that these analytical formulae are doomed to present numerical instability at high ℓ. Indeed, the expansion of the spherical Bessel functions in terms of powers of $1/x$ as in Eqs. C.4-C.5-C.6 is ill-advised at high ℓ, as it leads to delicate cancellations of the numerous terms, in particular for $x \leq \ell$. We thus expect that our analytical formulae for C_ℓ will also lead to delicate cancellations which may be numerically unstable. Another way of seeing this is to notice that, at high ℓ, we have from Limber's approximation that $C_\ell \propto P\,[k = (\ell + 1/2)/r(z)]$, and will thus be a decreasing function of ℓ. However we saw that $\alpha^{c,-}_{\ell,0} = 1$ and thus C_ℓ always contains a term $I^-_{c,0}/2 \approx C_0$. This term will hence need to be (at least partially) cancelled by higher order terms, and this cancellation will need to be increasingly precise at high ℓ, since $P(k)$ is a steep decreasing function of k.

Given these issues, in practice, we implemented this low multipole method only for $\ell = 0, 1, 2$, and used these to check our results obtained from the numerical method described in Sect. 4.3.